

DOI: 10.1002/adem.201200387

Wrinkling of Interfacial Layers in Stratified Composites**

By Yaning Li,[†] Narges Kaynia,[†] Stephan Rudykh and Mary C. Boyce*

Many structured composites in nature possess undulating and wrinkled interfacial layers that regulate mechanical,^[1] chemical,^[2] acoustic, adhesive,^[3] thermal, electrical,^[4,5] and optical functions,^[6,7] and also serve to reveal underlying physiological mechanisms in the diagnosis of diseases.^[8] As one example, the wavy layers of the silvery reflectors around the eyes of squid (*L. Pealeii*) facilitate broadband reflectance and result in silvery iridescence,^[6] providing inspiration for creating composite structures with different optical functions. Another example is the wavy elastica lamellae embedded in soft muscle in arterial walls which provides a diagnostic signature for disease. The degree of the elastica lamellae undulation was found to be significantly greater in persons with coronary artery disease compared to that found in the non-coronary disease group.^[8] Hence, understanding the mechanism governing the waveform formation can provide clues to other underlying structural, bio-chemical and mechanical changes. Furthermore, the ability to actively alter the interface structure can enable on-demand tunability of these attributes and functions to provide, for example, active control of wave propagation phenomenon (e.g., phononic and photonic), mechanical stiffness and deformation, and material swelling and growth.

In this investigation, we explore the mechanisms of the formation of wrinkled interfaces in soft multi-layered composites through experiments, analytical models and numerical simulations. Instabilities have been a subject of study in a number of composite material systems where structural mechanics approaches,^[9–11] energy methods,^[12] and Bloch wave analyses,^[13,14] have been found to predict this complex phenomenon. The main objective of this paper is to explore and predict instabilities in the interfacial layers of layered composites (details are provided in Supporting Information S1–S3). Prototypes of soft multi-layered polymer composites are

fabricated via a multi-material 3D-printer and mechanically tested, confirming the predictive design guidelines which are established through analytical and numerical models.

1. Results and Discussion

1.1. Wrinkling of an Interfacial Layer Embedded in a Compliant Matrix

Plane strain compression of different 3D-printed prototypes with a single interfacial layer of thickness t and modulus E_1 embedded in an elastomeric matrix with modulus E_0 (see Section 3) show the onset and evolution of wrinkling of the interfacial layers during compressive loading and also its reversibility upon unloading (Figure 1). The wrinkle onset, wavelength, and amplitude are seen to strongly depend on interfacial thickness (t) and the ratio of elastic moduli of the interfacial material to that of the matrix (E_1/E_0).

Consider the interfacial layer embedded in a compliant matrix to be subjected to a direct or indirect compressive stress, for example, through direct compression as in Figure 1, or indirectly through constrained contraction of the adjacent matrix and/or other internally generated turgor pressure. 3D-printed prototypes subjected to direct compression are shown in Figure 1. With an increase in the loading, the compressive stress in the interfacial layer will reach a critical value where bending will be energetically favored over simple compression resulting in the observed wrinkling of the interfacial layer.

The scaling of the critical wavelength with t and with E_1/E_0 are similar to that for the wrinkling of a stiff coating on a compliant substrate.^[15–20] Assuming a harmonic form for the lateral displacement of the interface, namely $w(x) = A \cos(2\pi x/\lambda)$, where A is the amplitude of the undulation, and λ is the wavelength of the undulation. The bending energy (per unit depth) of the interfacial layer scales as $U_b \propto (E_1 t^3 A^2)/\lambda^4$,^a whereas the local strain energy in the surrounding matrix scales as $U_s \propto (E_0 A^2)/\lambda$. Energy minimization results in scaling laws for the critical wavelength

[*] Dr. Y. Li

Department of Mechanical Engineering,
University of New Hampshire, Durham, NH, USA
N. Kaynia, Dr. S. Rudykh, Prof. M. C. Boyce
Department of Mechanical Engineering, Massachusetts
Institute of Technology,
Cambridge, MA 02139, USA
E-mail: mcboyce@mit.edu

[**] This work was supported primarily by the MIT MRSEC through the MRSEC program of the National Science Foundation (NSF) under award number DMR-0819762. Supporting Information is available from the Wiley Online Library or from the author.

[†] These authors contributed equally to this paper.

^aIn this paper, E_1 , ν_1 are the stiffness and Poisson's ratio of the interfacial layer, respectively. t is thickness of the interfacial layer. When the matrix is one material, E_0 and ν_0 are the stiffness and the Poisson's ratio of the matrix material; when the matrix on the two sides of the interfacial layer are two different materials, E_{01} and E_{02} are the stiffness of the two materials, and ν_{01} and ν_{02} are the Poisson's ratio of the two materials.

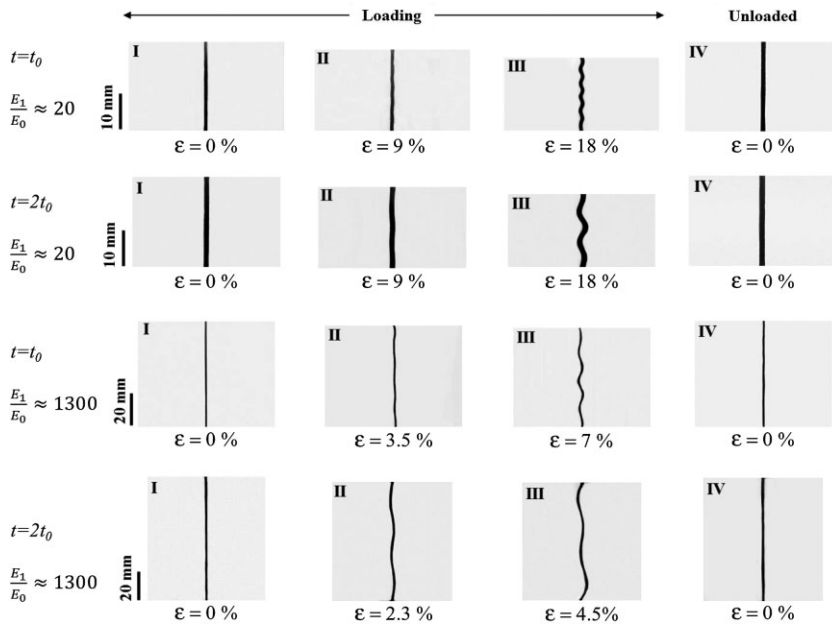


Fig. 1. Experimental results showing the onset and development of the wrinkling of a single interfacial layer embedded in softer matrix made of TangoPlus ($E_0 = 0.9$ MPa). (a) Specimen 1 (row 1) with interface thickness $t_0 = 0.5$ mm made of Digital Material ($E_1 = 18$ MPa), Specimen 2 (row 2) with $t_0 = 1$ mm made of Digital Material, Specimen 3 (row 3) with $t_0 = 0.5$ mm made of VeroWhite material ($E_1 = 1200$ MPa), Specimen 4 (row 4) with $t_0 = 1$ mm made of VeroWhite material.

$\lambda_{cr} \propto t(E_1/E_0)^{1/3}$ and the critical strain $\epsilon_{cr} \propto (E_1/E_0)^{-2/4}$. Beyond the scaling laws, closed-form solutions for the critical instability conditions are obtained by solving the governing differential equations^[9,21]:

$$D \frac{d^4 w}{dx^4} + \sigma t \frac{d^2 w}{dx^2} - \frac{t}{2} \frac{d\sigma_{xy}}{dx} = -\sigma_{yy} \quad (1)$$

where $D = (E_1 t^3)/12$ is the bending stiffness of the interfacial layer per unit depth and $w(x)$ is the deflection of the interfacial layer; σ is the compressive stress in the interfacial layer (Figure S1-1); σ_{yy} and σ_{xy} are the interfacial normal and shear traction components (Figure S1-2). Solving the differential equation and the boundary value problem (see Supporting Information S1), the critical strain ϵ_{cr} and the nondimensionalized wavelength λ_{cr}/t , corresponding to the onset of interfacial wrinkling are found to be:

$$\begin{cases} \epsilon_{cr} = \frac{\sigma_{cr}}{E_1} = C_\epsilon(v_0) \left(\frac{E_1}{E_0}\right)^{-2/3} \\ \frac{\lambda_{cr}}{t} = C_\lambda(v_0) \left(\frac{E_1}{E_0}\right)^{1/3} \end{cases} \quad (2a)$$

where, C_ϵ and C_λ are coefficients which for plane strain are given in Equations 2b and 2c (Plane stress given in Supporting Information S1):

$$C_\epsilon(v_0) = (3)^{2/3} \left[\frac{(3-4\nu_0)}{(1-\nu_0)^2} \right]^{-2/3} = 2.08 \left[\frac{3-4\nu_0}{(1-\nu_0)^2} \right]^{-2/3} \quad (2b)$$

$$C_\lambda(v_0) = \pi \left(\frac{1}{3}\right)^{1/3} \left[\frac{(3-4\nu_0)}{(1-\nu_0)^2} \right]^{1/3} = 2.18 \left[\frac{3-4\nu_0}{(1-\nu_0)^2} \right]^{1/3} \quad (2c)$$

The critical strain ϵ_{cr} and the non-dimensionalized wavelength λ_{cr}/t show, respectively, the $-2/3$ and $1/3$ power law scaling with the stiffness ratio E_1/E_0 as predicted earlier by the scaling law. Using Equations 2a–2c, the critical strain and wavelength can be expressed directly in terms of one another:

$$\epsilon_{cr} = \pi^2 \left(\frac{\lambda_{cr}}{t}\right)^{-2} \quad \text{or} \quad \frac{\lambda_{cr}}{t} = \frac{\pi}{\sqrt{\epsilon_{cr}}} \quad (3)$$

Since Equation 1 was derived from structural mechanics theory, the assumption of a thin structure needs to be satisfied, i.e., $(\lambda_{cr}/t) > \approx 8-10$, thus E_1/E_0 should be larger than ≈ 12.5 to 25.

The results of the analytical derivations were further examined by comparison to finite element (FE) simulations. FE simulation results of the wavy patterns of the interfacial layer are shown in Figure 2a, in which the deformed images are shown at a strain larger than the critical strain, ϵ_{cr} .

The map of deformed images (shown in Figure 2a) depicts the strong dependence of wavelength on both stiffness ratio and thickness. Figure 2b–2d compare the FE-, experimental- and analytical results, confirming the linear dependence on t and the exponential dependence on E_1/E_0 . These results show that the new analytical model is accurate for a large range of stiffness ratios. The results are further compared to the case for a coating on a compliant substrate,^[9,22,23] showing the interfacial layer to wrinkle at a higher critical strain, $(\epsilon_{cr}^{\text{interface}}/\epsilon_{cr}^{\text{coating}}) = (1/4)^{-1/3}$; and to yield a shorter wavelength, $(\lambda_{cr}^{\text{interface}}/\lambda_{cr}^{\text{coating}}) = (2)^{-1/3}$. The additional matrix constraint for the embedded interfacial layer leads to a higher matrix energy penalty and hence the shorter wavelength and higher critical strain.

When the onset of instability occurs at small strains, Equations 2a–2c for the critical wavelength are valid. However, when the critical strain is modest (e.g., a 5% critical strain will decrease the critical wavelength by approximately 5%), the increased thickness of the interface layer due to axial strain should be taken into account. Assuming the overall contour length of the interface is preserved, the post-buckling wavelength λ and amplitude A are obtained from kinematics:^[22]

$$\lambda(\epsilon) = \lambda_{cr} e^{(-\epsilon)}, \quad \epsilon > \epsilon_{cr} \quad (4a)$$

$$A(\epsilon) = \frac{\lambda(\epsilon)}{\pi} \sqrt{|\epsilon - \epsilon_{cr}|} \quad \epsilon > \epsilon_{cr} \quad (4b)$$

The post-wrinkling wavelengths of those Specimens (Figure 1) were compared with the analytical prediction using Equations 2a–2c, 4a, and 4b, as shown in Figure 2d. It can be seen that Equations 2a–2c, 4a, and 4b capture the onset of wrinkling and the mechanism of wrinkle developments

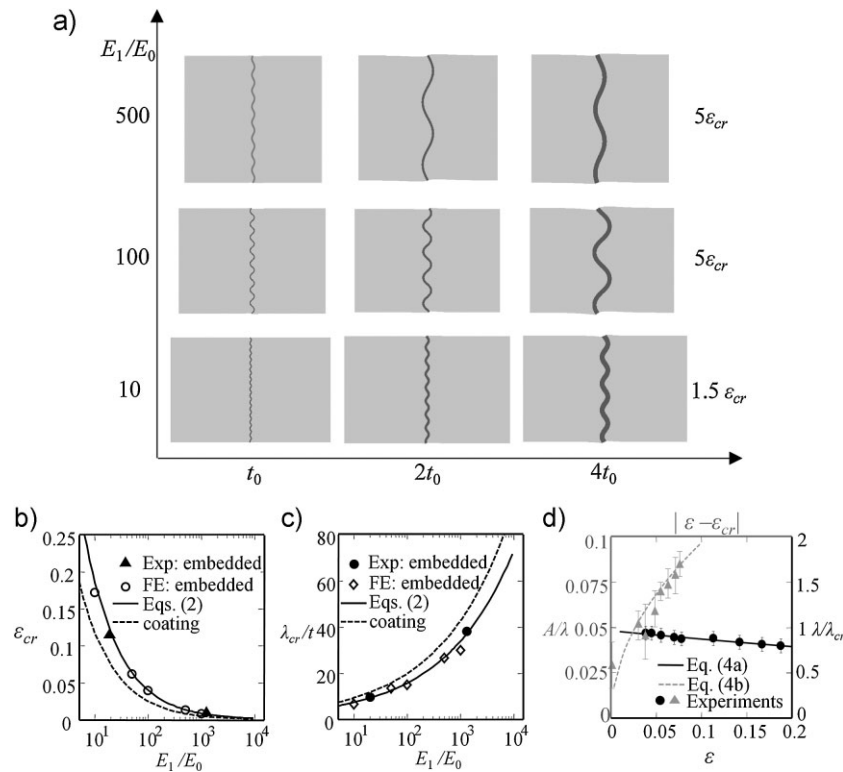


Fig. 2. Comparison of the results of analytical, FE simulations and mechanical experiments for the dilute cases, (a) FE simulation results; (b) comparison of the analytical (Equations 2a–2c) and FE simulation results of critical strain versus stiffness ratio; and (c) comparison of the analytical (Equations 2a–2c) and FE results of the nondimensional wavelength versus stiffness ratio, (d) comparison of the analytical (Equations 4a and 4b) and experimental results of the post-wrinkling wavelength.

during the post-buckling process accurately. The case of a single interfacial layer embedded between two different matrix media follows a similar derivation and is shown together with FE results in Supporting Information S3.

1.2. Instability of Multi-Layered Composites

We now consider a multi-layered composite where interfacial layers of thickness, t , are separated by a distance, d . The distance-to-thickness ratio, d/t , is found to govern two different modes of instability:

- (I) The dilute case (wrinkling instability): when d/t is large (will be specified quantitatively later), the matrix stress fields emanating from neighboring layers do not interact, hence the shear term in Equation 1 is negligible and interfacial layers behave independently of one another. Therefore, the buckling results in wrinkling of the interfacial layers and follows the analysis of an isolated interfacial layer given earlier.
- (II) The concentrated case (long-wave instability): when d/t is small, the matrix stress fields overlap and the matrix shear stress is no longer negligible and governs the instability. In this case, the instability induced deformations are not localized at the interfaces and a cooperative long-wave instability mode occurs.

For the concentrated case, the long-wave mode for a multi-layered composite where the two phases buckle together was derived by Rosen using the energy method

and assuming a shear mode deformation.^[12] Further studies were also reported which provide a more general solution taking into account both the normal stress and shear stress terms in Equation 1.^[9,10] For the plane strain case, the critical strain at which the long-wave mode occurs as predicted by Rosen is given by:^[12]

$$\varepsilon_{cr}^{\text{Longwave}} = \frac{1}{2(1 + \nu_0)} \frac{d^2}{t(d - t)} \left(\frac{E_1}{E_0} \right)^{-1} \quad (5)$$

By equating the critical strain in Equations 2a and 5, the critical layer distance to thickness ratio d^*/t at which the instability transitions from a wrinkling form of instability to a cooperative long-wave instability is:

$$\frac{d^*}{t} = \left\{ 0.5 - \sqrt{0.25 - 0.24(3 - \nu_0)^{2/3} (1 + \nu_0)^{-(1/3)} \left(\frac{E_1}{E_0} \right)^{-(1/3)}} \right\}^{-1} \quad (6)$$

Alternatively, this equation gives a relationship between the critical distance between the layers, d^* , and the critical buckling wavelength λ_{cr} (shown in Equations 2a–2c):

$$d^* = \frac{1.92}{3 - \nu_0} \lambda_{cr}^* \approx 0.77 \lambda_{cr}^*$$

This shows that if the distance between layers $d < 0.77 \lambda_{cr}$, then the layers start to interact and the shear stress

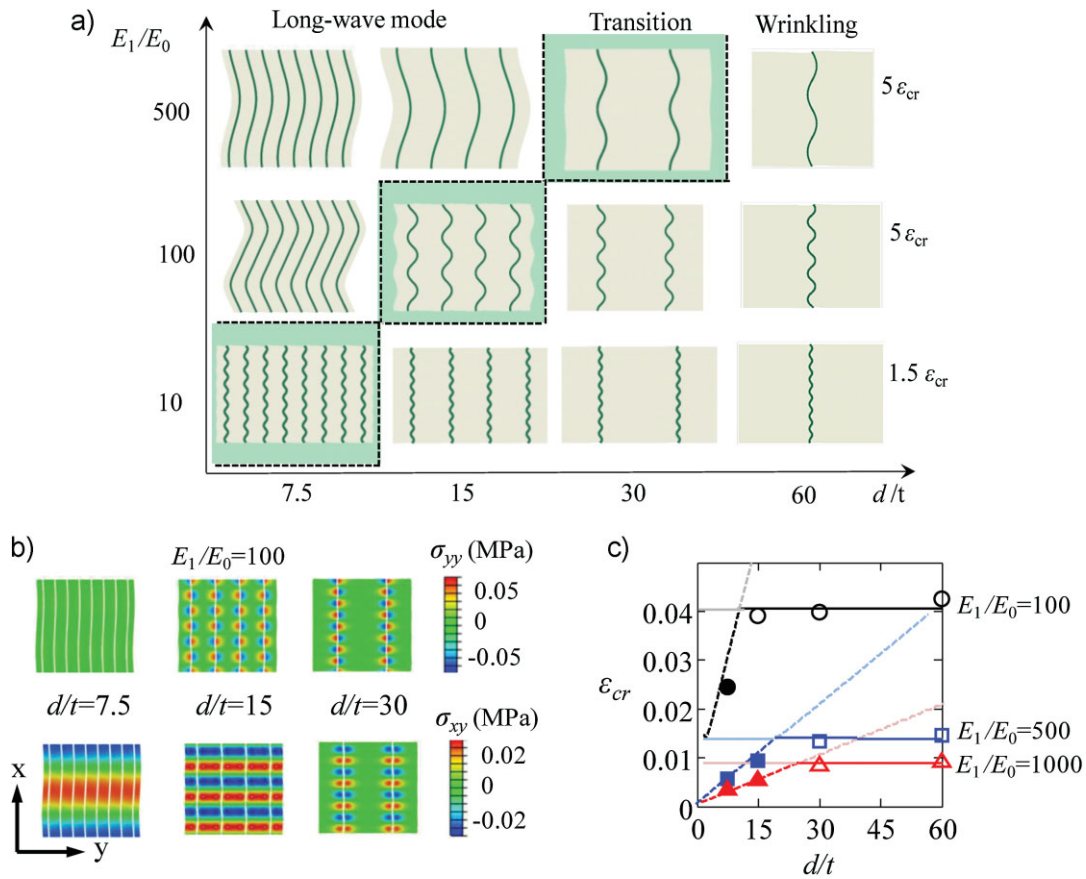


Fig. 3. Mode transition mechanisms for multi-layered composites from a dilute case to a concentrated case, (a) FE results of layers with different d/t and E_1/E_0 ; (b) normal and shear stress contours for the case of $E_1/E_0=100$ and three d/t cases showing the transition from local wrinkling to global long-wave instability; and (c) phase diagram indicating the condition for mode transition (solid lines represent the case of wrinkling via Equations 2a–2c, dashed lines represent the case of long-wave mode via Equation 5, the darker parts of these lines represent when the mode occurs).

contribution becomes significant such that a cooperative long-wavelength mode of instability will occur.

The transition from wrinkling to cooperative long-wave instability is shown in the simulation results of Figure 3 and the experimental results of Figure 4. FE simulation results for different d/t and with various stiffness ratios E_1/E_0 between the two phases illustrate the transition from wrinkling to long-wave mode. It can be seen that when the stiffness ratio increases and/or the distance between layers decreases, the instability mode transits from a local wrinkling mode to a long-wave mode. Focusing on the case of $(E_1/E_0)=100$, Figure 3b shows the transition in the normal and shear stress fields for $d/t = 7.5, 15$ and 30 : as d/t decreases, the stress fields begin to overlap and the matrix shear leads to the transition to a long wavelength instability.

Figure 3c shows that wrinkling becomes the more prevalent instability mode when the stiffness ratio decreases. For smaller stiffness ratios only very small intervals of d/t will result in long-wavelength modes of instability. The general transition between wrinkling and long wavelength modes is shown in Figure 3c, giving a design guideline for choosing material properties and layer spacing to

provide transforming, wrinkling interface structures upon deformation.

The dependence of the wrinkling and long-wave mode instabilities on E_1/E_0 and d/t is further demonstrated in the experimental results of Figure 4. Specimen 1 [$d/t=20$; $E_1/E_0=20$] shows a wrinkling mode, while Specimen 3 [$d/t=20$; $E_1/E_0=1300$] shows the influence of a much greater stiffness ratio at the fixed spacing and shows the transition to a long-wave mode. Both results are in agreement with model predictions. Finally, Specimen 2 [$d/t=6$; $E_1/E_0=20$] shows a case with the same stiffness ratio as Specimen 1, but reduced spacing: the model predicts this case to be located at the transition meaning it could either wrinkle or buckle in a long wave mode and it is sensitive to perturbation (imperfection, boundary conditions, etc.); here a cooperative wrinkle is observed. These results demonstrate the predictive capability of the model and hence its use as a guideline for material designs.

The results of the transition in instability mode from wrinkling to long-wave mode are shown in the transition envelope of Figure 4b. Here, the curves give the analytical model prediction of the transition envelope from long-wave mode to wrinkle mode and shows how the modes found in the

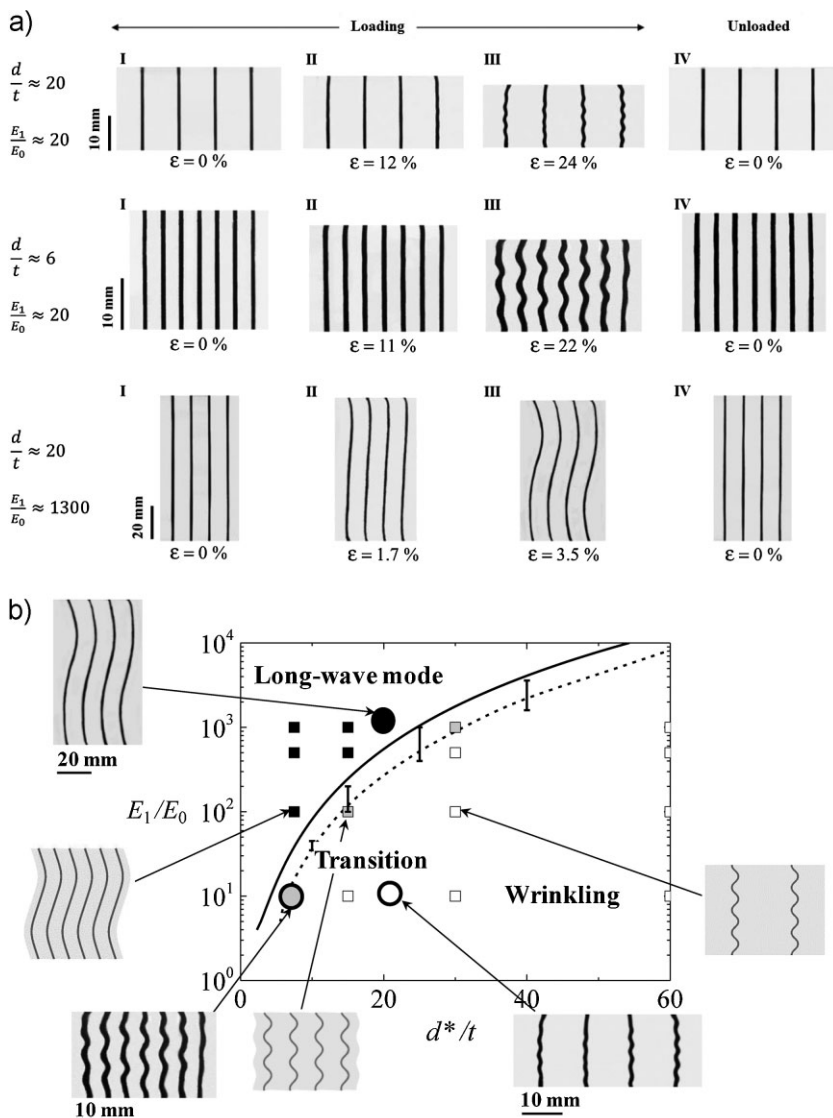


Fig. 4. (a) Results of the mechanical experiments of the formation and development of the wrinkling of multi-layered composites: Specimen 1 (row 1) $E_1/E_0=20$ and $d/t=20$; Specimen 2 (row 2) $E_1/E_0=20$ and $d/t=6$; Specimen 3 (row 3) $E_1/E_0=1300$ and $d/t=20$; and (b) predictive instability transition envelope showing the transition from wrinkling to long wave mode as a function of E_1/E_0 and d/t ; comparison of the results of analytical prediction (solid line Equation 6), Bloch wave analysis (dash line with error bars, details can be found in Supporting Information S4), FE simulations (hollow symbols), and mechanical experiments (solid symbols) for multi-layered composites.

FE and experimental results fall with respect to this envelope. Again, excellent agreement is shown, supporting the predictive design guidelines.

2. Conclusions

The analytical models together with the numerical approaches provide the ability to derive biomimetic principles for active and multi-functional hybrid materials or actuating devices, or functionally graded materials. In particular, the direct outcomes of this deformation-induced and mechanically tunable interfacial boundary include the change in the morphology of the interfaces and its impact on the overall mechanical and multi-functional performance of the layered

structure together with the increased interfacial area per unit length on other properties (e.g., interfacial transport and signaling). By tailoring the choice of material properties, relative geometry (d/t), and the geometric lengthscale, potential applications are expected to be found in the design of mechanically tunable multi-layer reflectors for structural colouration and camouflage,^[7] and for acoustic filters, and thermoregulation. In addition, the modeling results can provide deeper insights into the morphogenesis and phenotype diversity of wrinkling interfacial pattern in natural systems.^[1,8]

3. Experimental

3.1. Materials

Single- and multi-layered composite material prototypes were fabricated with a multi-material 3D-printer (Object Connex500 at MIT). Two base polymers were used in printing: an acrylic-based photo-polymer, VeroWhite (Young's Modulus 1.2 GPa, referred to here as VW), and a rubbery material, TangoPlus (initial Young's Modulus 0.9 MPa, referred to here as TP). The matrix phase was always printed in TangoPlus, while the interfacial layers were printed in VeroWhite and also in "Digital Material" which is a mixture of the two base materials (Young's Modulus 18 MPa, referred to here as DM).

3.2. Single Interfacial Layer Prototypes

Composites consisting of one centrally located single interfacial layer of either VW or DM embedded in TP were fabricated (Figure 5a). The thickness of the interfacial layer was set to both $t_0=0.5$ mm and $t_0=1$ mm, where we note that the resolution of the 3D printer robustly provides for interface thicknesses of 0.25 mm and larger. The planar dimensions of the specimens with VW interfacial layers were 81 mm \times 88 mm (width \times height), chosen to minimize any influence of edge boundary conditions on the resulting instability patterns. The specimens with DM interfaces were 41 mm \times 33 mm (width \times height). The out-of-plane dimension (depth) was 12 mm for all specimens.

3.3. Multi-Layered Prototypes

Specimens with multiple interfacial layers were fabricated. The interfacial layer thickness was kept constant at $t_0=0.5$ mm, while the distance between the layers was set to be $d=10$ mm for the VW interface specimens, and $d=10$ and 3 mm for the DM interface specimens. The height of the VW interface specimens were 88 mm and the DM interface specimens were 33 mm. The out-of-plane dimension was again 12 mm for all specimens.

3.4. Mechanical Experiment

Plane strain compression tests were performed using a screw-driven Zwick Mechanical Tester. The specimens were placed in a

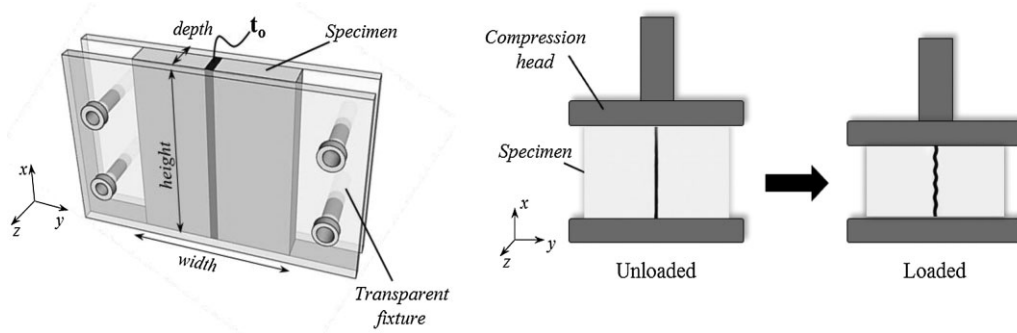


Fig. 5. Experimental setup of a single interfacial layer specimen with dimension definitions. The transparent fixture prevents deformation in the z-direction assuring plane strain conditions.

transparent fixture restricting the deformation in the out-of-plane direction so that the plane strain conditions were imposed (Figure 5). Mineral oil was used as a lubricant between the specimens and the fixture to provide near frictionless conditions. The experiments were directly monitored during testing using a camera; this also allowed measurement of the axial strain using Digital Image Correlation (DIC). The tests were performed quasi-statically with a nominal engineering strain rate of 0.00015 s^{-1} for the DM interface specimens and 0.000057 s^{-1} for the VW interface specimens.

Received: December 18, 2012
Final Version: March 18, 2013
Published online: May 2, 2013

- [1] J. R. Puzey, S. J. Gerbode, S. A. Hodges, E. M. Kramer, L. Mahadevan, *Proc. R. Soc. B* **2011**, 279, 1640.
- [2] K. Koch, B. Bhushan, W. Barthlott, *Prog. Mater. Sci.* **2009**, 54, 137.
- [3] E. P. Chan, E. J. Smith, R. C. Hayward, A. J. Crosby, *Adv. Mater.* **2008**, 20, 711.
- [4] L. Baggetto, D. Danilov, P. H. L. Notten, *Adv. Mater.* **2011**, 23, 1563.
- [5] T. K. Bhandakkar, H. T. Johnson, *J. Mech. Phys. Solids* **2012**, 60, 1103.
- [6] L. M. Mathger, E. J. Denton, N. J. Marshall, R. T. Hanlon, *J. R. Soc. Interface* **2009**, 6, S149.
- [7] A. R. Parker, *J. Opt. A: Pure Appl. Opt.* **2000**, 2, R15.
- [8] E. S. Mortensen, T. O. Rognum, B. Straume, L. Jørgensen, *Cardiovasc. Pathol.* **2007**, 16, 336.
- [9] H. G. Allen, *Analysis and Design of Structural Sandwich Panels*, Pergamon, New York **1969**, Ch. 8.
- [10] R. Parnes, A. Chiskis, *J. Mech. Phys. Solids* **2002**, 50, 855.
- [11] M. Gei, *Eur. J. Mech. A/Solids* **2008**, 27, 328.
- [12] B. W. Rosen, *Fiber Composite Materials*, American Society for Metals, Metals Park, OH **1965**, Ch. 3.
- [13] N. Triantafyllidis, B. N. Maker, *Trans. ASME* **1985**, 52, 794.
- [14] K. Bertodi, M. C. Boyce, S. Deschanel, S. M. Prange, T. Mullin, *J. Mech. Phys. Solids* **2008**, 56, 2642.
- [15] E. Cerda, L. Mahadevan, *Phys. Rev. Lett.* **2003**, 90, 074302.
- [16] L. Wang, C.-L. Pai, M. C. Boyce, G. C. Rutledge, *Appl. Phys. Lett.* **2009**, 94, 1916.
- [17] X. Chen, J. Yin, *Soft Matter*. **2010**, 6, 5667.
- [18] H.-S. Kim, A. J. Crosby, *Adv. Mater.* **2011**, 23, 4188.
- [19] J. Y. Chung, A. J. Nolte, M. Stafford, *Adv. Mater.* **2009**, 21, 1358.
- [20] J. Y. Chung, A. J. Nolte, C. M. Stafford, *Adv. Mater.* **2011**, 23, 349.
- [21] N. Bowden, S. Brittain, A. G. Evans, J. W. Hutchinson, M. Whitesides, *Nature* **1998**, 393, 146.
- [22] X. Chen, J. W. Hutchinson, *J. Appl. Mech.* **2004**, 71, 597.
- [23] J. Yin, J. L. Yague, D. EggenSpieler, K. K. Gleason, M. C. Boyce, *Adv. Mater.* **2012**, 24, 5441.